JOURNAL OF SPACECRAFT AND ROCKETS
Vol. 29, No. 1, January–February 1992

Improved Nonequilibrium Viscous Shock-Layer Scheme for Hypersonic Blunt-Body Flowfields

Bilal A. Bhutta* and Clark H. Lewis†
VRA, Inc., Blacksburg, Virginia 24063

The nonequilibrium viscous shock-layer (VSL) solution scheme is revisited to improve its solution accuracy in the stagnation region and also to minimize and control errors in the conservation of elemental mass. The stagnation-point solution is improved by using a second-order expansion for the normal velocity, and the elemental mass conservation is improved by directly imposing the element conservation equations as solution constraints. These modifications are such that the general structure and computational efficiency of the nonequilibrium VSL scheme is not affected. This revised nonequilibrium VSL scheme is used to study the Mach 20 flow over a 7-deg sphere-cone vehicle under 0- and 20-deg angle-of-attack conditions. Comparisons are made with the corresponding predictions of Navier-Stokes and parabolized Navier-Stokes solution schemes. The results of these tests show that the nonequilibrium blunt-body VSL scheme is indeed an accurate, fast, and extremely efficient means for generating the blunt-body flowfield over spherical nose tips at zero-to-large angles of attack.

Nomenclature

C_i = mass fraction of the ith species
Cp = nondimensional specific heat at constant pressure, Cp^*/Cp^*_∞
D_i = nondimensional binary diffusion coefficient for the ith species, $D_i^* \rho^*_\infty/\mu^*_{\text{ref}}$
E_e = mass fraction of the eth element
h_{11} = scale factor, $(1 + \eta n_{\text{sh1}})$
k = nondimensional thermal conductivity, $k^*/\mu^*_{\text{ref}} Cp^*_\infty$
Le = Lewis number, $\rho CpD_i/k$
M = Mach number
NE = total number of elements
NS = total number of chemical species
n = nondimensional surface-normal coordinate n^*/Rn^*
n_{sh1} = first-order term in the expansion of n_{sh}
P, p = nondimensional pressure, $p^*/\rho^*_\infty (V^*_\infty)^2$
$PINF$ = freestream static pressure, p_∞
Pr = Prandtl number, $\mu Cp/k$
PW = wall pressure, p_w
QW = wall heat transfer rate, Btu/ft^2/s
R = radial distance from body axis
RB = local body radius
Re = Reynolds number, $(\rho VRn)/\mu$
RN, Rn = nose radius
S, s = nondimensional streamwise coordinate, s^*/Rn^*
T = nondimensional temperature, T^*/T^*_{ref}
T^*_{ref} = dimensional reference temperature, $(V^*_\infty)^2/Cp^*_\infty$
u = nondimensional streamwise velocity, u^*/V^*_∞
V = total velocity
v = nondimensional body-normal velocity, v^*/V^*_∞
w = nondimensional crossflow velocity, w^*/V^*_∞
X, x = coordinate along body axis
α = angle of attack, deg
ϵ = Reynolds number parameter, $[\mu^*_{\text{ref}}/\rho^*_\infty V^*_\infty Rn^*]^{0.5}$
ζ = crossflow coordinate, ϕ
η = normalized body-normal coordinate, n/n_{sh}
μ = nondimensional viscosity, μ^*/μ^*_{ref}
μ^*_{ref} = dimensional viscosity evaluated at T^*_{ref}
ξ = streamwise coordinate, s
ρ = nondimensional density, ρ^*/ρ^*_∞
ϕ = circumferential angle measured from the windward side

Subscripts

ref = reference quantity
sh = shock quantity
w = wall quantity
, = partial derivative
∞ = freestream quantity

Superscripts

– = quantity scaled with respect to the corresponding shock value
* = dimensional quantity

Introduction

OVER the last several years, the prediction of high-altitude (>120 kft) hypersonic re-entry flows has become an area of significant interest and development. At such high altitudes, the characteristic reaction time is much longer than the characteristic flow time, and the vehicle is in the chemical nonequilibrium flow regime for most of the time.

Existing computational fluid dynamics (CFD) schemes for predicting nonequilibrium hypersonic blunt-body flows can be broadly classified as 1) boundary-layer methods, 2) viscous shock-layer (VSL) methods, and 3) Navier-Stokes methods. High-altitude hypersonic re-entry flows are, in general, characterized by low Reynolds numbers. Because of such typically low Reynolds number flows, the application of boundary-layer methods (such as the scheme of Blottner et al.[1]) encounters significant numerical difficulties (such as displacement-thickness interaction, streamline tracking, determination of edge conditions, etc.). As far as nonequilibrium Navier-Stokes methods are concerned, over the last few years a number of such schemes have become available.[2-4] However, such methods are typically very time consuming and not well suited for practical design and analysis studies.

On the other hand, the nonequilibrium VSL blunt-body methods have shown great potential for analyzing such nonequilibrium viscous re-entry flows. Various studies over the last 15 years[5-14] have shown that the VSL scheme provides a very effective tool for accurately and efficiently predicting the

Received Feb. 21, 1991; revision received July 15, 1991; accepted for publication Aug. 5, 1991.

*Chief Scientist. Senior Member AIAA.
†President. Associate Fellow AIAA.

flowfield in regions where the flow is attached in the crossflow region. Although the VSL schemes cannot be used in regions of crossflow separation, even under large angle-of-attack conditions the flowfield in the nose region typically remains attached in the crossflow direction. Consequently, the VSL schemes can still be used to provide the necessary starting solution to initiate the afterbody parabolized Navier-Stokes (PNS) solution technique. Although reliable nonequilibrium Navier-Stokes schemes have recently become available, the nonequilibrium VSL blunt-body method can accurately predict the blunt-body flowfield for a small fraction of the computing time required by these Navier-Stokes schemes.

Recently, some comparisons between the predictions of the nonequilibrium VSL scheme of Swaminathan et al.[7] and the nonequilibrium Navier-Stokes predictions of Molvik and Merkle[2] were made by Buelow et al.[15] The flowfield accuracy of the corresponding perfect-gas and equilibrium-air VSL scheme has been recently confirmed by Edwards and Flores[16] and Ryan et al.[17] by comparing VSL results with the predictions of the compressible Navier-Stokes (CNS) code. The recent nonequilibrium comparisons of Buelow et al.[15] were, however, not satisfactory. In this case, Navier-Stokes and VSL methods were used to provide starting solutions for PNS afterbody schemes, and species profiles were compared at an axial location of 10 nose radii. The freestream flow corresponded to a Mach 20 re-entry at an altitude of 175 kft, and the geometry consisted of a 7-deg sphere-cone with a nose radius of 2 in. This axisymmetric case was based on an earlier 20-deg angle-of-attack case studied by Bhutta and Lewis.[18] The results of Buelow et al.[15] showed that although the wall-pressure and shock-shape predictions of the nonequilibrium VSL and nonequilibrium Navier-Stokes schemes agreed quite well in the blunt-body region, the species profiles at the body end did not. Buelow et al.[15] accepted this wall-pressure and shock-shape agreement in the blunt-body region as a check of the blunt-body flow and, thus, incorrectly concluded that the disagreement at the body end was due to some error in the nonequilibrium PNS scheme of Bhutta and Lewis[18,19] and Bhutta et al.[20] In this paper, we have studied this case in more detail, and our results indicate that the differences observed in the species profiles at the body end were actually due to the differences in the flowfield chemistry in the blunt-body region and not caused by the afterbody PNS calculations.

One of the main objectives of this paper is to revisit the nonequilibrium blunt-body VSL scheme in order to improve the VSL predictions and resolve the observed disagreement between the nonequilibrium VSL/PNS and Navier-Stokes predictions. In the absence of experimental data, an important measure of the numerical accuracy of a nonequilibrium blunt-body solution is the accuracy to which it satisfies global conservation of elemental mass. The VSL scheme historically has been formulated in a nonconservative form. Although the global conservation of mass is enforced by adjusting the local shock standoff distance, there is no direct means of controlling the nonconservative errors in the individual species conservation equations that are reflected in the global conservation of elemental mass. The results of this study show that, in some cases, these errors in the global conservation of elemental mass can be larger than the error in the global conservation of mass. It is important to note that these nonconservative errors are present in all nonequilibrium VSL schemes developed to date by various researchers (such as Moss,[5] Miner and Lewis,[6] Swaminathan et al.,[7] Shinn et al.,[8] Kim et al.,[9] Song and Lewis,[10] Thompson,[11] Gupta,[12] and Zoby et al.[13]). In most instances, with these nonequilibrium VSL schemes, the conservation of elemental mass may vary from good to satisfactory, depending on the accuracy with which the global conservation of mass is satisfied. However, this is not automatically guaranteed for every case because of the errors due to 1) numerical inaccuracies, 2) nonconservative VSL formulation, and 3) the fact that the conservation of element mass fraction is not directly imposed.

The major focus of this paper is to present some recent improvements in the nonequilibrium VSL blunt-body solution scheme. Briefly speaking, these improvements involve enhancements to the spherical stagnation-point solution and the reduction of the nonconservative numerical errors in element conservation by directly imposing the conservation of element mass. A direct imposition of these element conservation equations does not affect the global conservation of mass; however, it does improve the conservation of mass of the individual elements. Detailed comparisons of these improved nonequilibrium VSL predictions have also been done with the corresponding predictions of the nonequilibrium Navier-Stokes scheme in terms of the flowfield and species profiles as well as the surface-measurable quantities.

Solution Scheme

The VSL equations for a chemically reacting binary gas mixture were originally derived from the full Navier-Stokes equations by Davis.[21] Moss[22] further extended the VSL scheme to study a five-species (O, O_2, N, N_2, and NO) gas model. However, these studies were restricted only to analytic bodies such as hyperboloids. Miner and Lewis[6] extended the VSL scheme to study axisymmetric flows over nonanalytic (sphere-cones) re-entry vehicles using the seven-species (O, O_2, N, N_2, NO, NO^+, and e^-) model of Blottner et al.[1]

Swaminathan et al.[23,24] further extended the nonequilibrium VSL scheme to study the three-dimensional nonequilibrium viscous flows over multiconic re-entry vehicles. To do so, they used the earlier approach of Waskiewicz and Lewis[25] to couple the first-order continuity and normal-momentum equations, resulting in increased stability of the three-dimensional VSL solution scheme. Kim et al.[9,26] extended the nonequilibrium VSL scheme to a general surface-orthogonal coordinate system to study the nonequilibrium flow over the Space Shuttle. All of these nonequilibrium VSL schemes used a scalar (uncoupled) solution of the species conservation equations in which the coupling of the production terms with other species is neglected, and each species conservation equation is solved independent of others.

The governing VSL equations are derived from the steady Navier-Stokes equations for the axisymmetric flow of a multicomponent reacting gas mixture[27] written in terms of the surface-normal coordinate system shown in Fig. 1, where the s coordinate is tangent to the body in the streamwise direction, the n coordinate is normal to the surface, and the ϕ coordinate is measured from the windward to the leeward pitch plane.

These governing Navier-Stokes equations are first normalized by variables that are of order 1 at the body surface, and

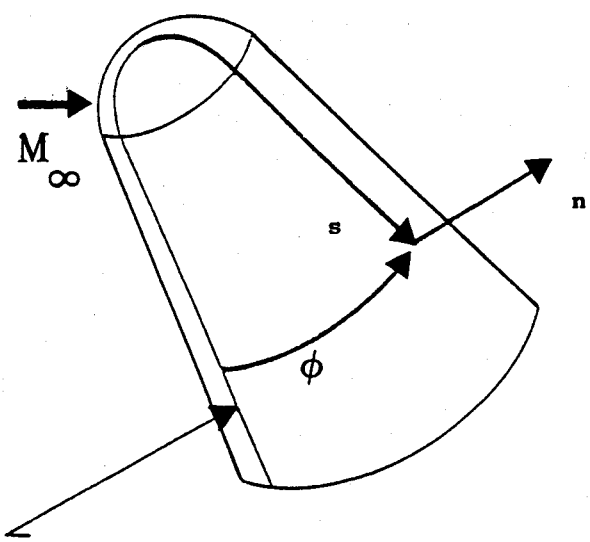

Fig. 1 Coordinate system.

they are then again normalized by variables that are of order 1 at the outer bow shock. The VSL equations are then obtained from these Navier-Stokes equations by neglecting terms higher than second order [$\mathcal{O}(\epsilon^2)$]. Consequently, the VSL equations are uniformly second-order accurate from the body to the shock. Furthermore, the resulting nonequilibrium VSL equations are also parabolic in the streamwise and crossflow directions.

In the normalized surface-normal coordinate system (ξ, η, ζ), the conservation equations for s momentum, ϕ momentum, energy, and species mass fraction are written in the standard parabolic form:

$$A_0 W_{,\eta\eta} + A_1 W_{,\eta} + A_2 W + A_3 + A_4 W_{,\xi} + A_5 W_{,\zeta} = 0 \qquad (1)$$

where W is the dependent variable (u, w, T, and (C_i) in the s momentum, ϕ momentum, energy, and the species conservation equations, respectively).

The continuity and normal momentum equations are first-order differential equations and, when solved independently, pose numerical difficulties especially when surface discontinuities (such as at the nose-afterbody tangent point) are involved. However, using the coupling approach developed by Waskiewicz and Lewis,[25] these two first-order equations are coupled together to form a second-order system that can be solved using a tridiagonal solution procedure. This numerical coupling considerably enhances the overall numerical stability of the VSL solution scheme and makes it possible to treat geometric discontinuities.

The finite difference algorithm used to solve these flowfield equations is based on the scalar tridiagonal approach developed by Murray and Lewis[28] for perfect-gas flows and by Swaminathan et al.[23,24] and Kim et al.[9,26] for finite rate chemically reacting flows.

All of the existing nonequilibrium VSL blunt-body schemes[5-14] use Blottner's linearization approach[2,6] to treat the rate-of-production term, where the production term appearing in a particular species conservation equation is linearized such that only that species concentration appears as the unknown. Furthermore, the production terms in the energy equation are also linearized such that the temperature appears as the only unknown.[2,6] In this manner, all equations can be solved uncoupled from each other. The detailed derivation of the conventional uncoupled VSL equations for a chemically reacting air mixture was given by Swaminathan et al.[23,24]

Briefly speaking, the VSL solution begins on the spherically blunted nose by first solving the governing equations along the stagnation streamline where the governing equations have a removable singularity, which is removed by using a series expansion of the flowfield variables around the stagnation streamline. Once the solution along the stagnation streamline has been obtained, the governing axisymmetric VSL equations are solved using a two-point backward-differenced approximation for the streamwise derivatives. At each marching step, the solution is iterated until it converges, and then the numerical solution steps downstream to obtain the solution at the next streamwise s station.

Because of the normalization with respect to the variables that are order 1 at the shock, the VSL equations depend on the shock slope $n_{\mathrm{sh},\xi}$ and the streamwise gradients of the flowfield variables behind the shock. In the present VSL approach, the shock slope ($n_{\mathrm{sh},\xi}$) over the solution domain is provided as input and is obtained using an appropriate inviscid solution scheme. The streamwise gradients of the flowfield behind the bow shock are then obtained internally using the local shock slope and two-point backward-differenced approximations. Although the shock slope is kept fixed during the solution iterations, after each iteration the local shock standoff distance is updated by imposing the global conservation of mass. In general, if needed, an appropriate number of global iterations can be done to further improve the input shock shape. However, no global iterations were done in the present study.

Imposing the Conservation of Element Mass

In the present approach, the mass-fraction distribution of the NE elements (E_e) across the shock layer is obtained from the governing element conservation equations. The VSL element conservation equations are obtained in a manner very similar to the species conservation equations. Even the form of these element conservation equations is identical to the species conservation equations, except for the absence of any production terms. Consequently, these element conservation equations are truly uncoupled from each other, and they are solved as such. Furthermore, since all of the elemental mass fractions at a point must add up to unity, we only solve $NE-1$ element conservation equations, and the last element's mass fraction is determined from this conservation constraint.

The element conservation equations can also be written in the following standard parabolic form

$$A_0 E_{e,\eta\eta} + A_1 E_{e,\eta} + A_4 E_{e,\xi} + A_5 E_{e,\zeta} = 0 \qquad (2a)$$

where E_e is the mass fraction of the eth element, and $e = 1, 2, \ldots, NE-1$.

For these element conservation equations the boundary conditions at the outer bow shock correspond to a frozen shock crossing [$(E_e)_{\mathrm{sh}} = (E_e)_\infty$]. At the wall, the correct wall boundary condition for these element conservation equations consists of the convection of elements away from the wall and diffusion of the elements toward the wall. This convection-diffusion boundary condition is in fact a first-order differential equation written as

$$\bar{\rho}_w v_w [(E_e)_w - (E_e)^-] = \epsilon^2 \left(\frac{\mu_{\mathrm{sh}} \bar{\mu} Le}{n_{\mathrm{sh}} Pr}\right)_w [E_{e,\eta}]_w \qquad (2b)$$

where $(E_e)^-$ is the elemental mass fraction of the injectant gas.

The solution scheme consists of first obtaining the mass fractions of $NS - NE - 1$ relatively less dominant species from the species conservation equations. Then the $NE-1$ number of element conservation equations [Eqs. (2a)] are solved to provide the following $NE-1$ algebraic constraint equations representing the local conservation of element mass

$$\sum_{i=1}^{NS} \left[\frac{(\alpha_e)_i A_e}{M_i}\right] C_i = E_e \qquad (3a)$$

where $(\alpha_e)_i$ is the number of atoms of element e in species i, A_e is the atomic weight of element e, and M_i is the molecular weight of species i. The last constraint equation is simply

$$\sum_{i=1}^{NS} C_i = 1 \qquad (3b)$$

Now Eqs. (3) represent NE number of algebraic equations that need to be solved to determine the mass fractions of the remaining NE species. For example, for the present case of seven-species clean air, the mass fractions of O, N, NO, and NO^+ were obtained from the corresponding species conservation equations, the mass fraction of O_2 was obtained from Eq. (3a), and that of N_2 was obtained from Eq. (3b). Note that the electrons (NSth species) have negligible mass.

Solution Improvements Along the Stagnation Streamline

The flowfield along the spherical stagnation streamline ($\xi = 0$) involves a removable singularity that can be removed by expanding all quantities around the spherical stagnation streamline ($\xi = 0$) in powers of ξ. In most of the existing VSL schemes,[5,6,22,28] first-order expansions were used for all variables except pressure p and shock standoff distance n_{sh}. Now the pressure field along this stagnation streamline is closely related to the normal velocity v. Thus, in the present approach, we have used a second-order expansion for the normal

velocity v. Thus, the flowfield variation around the stagnation streamline is expressed as

$$\begin{aligned}
\bar{\rho}(\xi,\eta) &= [\bar{\rho}_1(\eta)] + \cdots \\
\bar{u}(\xi,\eta) &= [\bar{u}_1(\eta)] + \cdots \\
v(\xi,\eta) &= [v_1(\eta)] + [v_2(\eta)]\xi^2 + \cdots \\
\bar{T}(\xi,\eta) &= [\bar{T}_1(\eta)] + \cdots \\
\bar{p}(\xi,\eta) &= [\bar{p}_1(\eta)] + [\bar{p}_2(\eta)]\xi^2 + \cdots
\end{aligned} \tag{4}$$

The corresponding shock quantities appearing in the governing equations are expanded as

$$\begin{aligned}
\rho_{sh}(\xi) &= \rho_{sh1} + \cdots \\
u_{sh}(\xi) &= u_{sh1}\xi + \cdots \\
n_{sh}(\xi) &= n_{sh1} + n_{sh2}\xi^2 + \cdots \\
T_{sh}(\xi) &= T_{sh1} + \cdots \\
p_{sh}(\xi) &= p_{sh1} + p_{sh2}\xi^2 + \cdots
\end{aligned} \tag{5}$$

By using these expansions along the stagnation streamline in the n-momentum equation, we can obtain the following improved expression for $\bar{p}_{2,\eta}$:

$$\begin{aligned}
\frac{\partial \bar{p}_2}{\partial \eta} = &\left\{ \frac{\rho_{sh1} u_{sh1}^2 n_{sh1} \bar{\rho}_1 \bar{u}_1^2}{p_{sh1}(1+\eta n_{sh1})} + \frac{2\rho_{sh1} u_{sh1} n_{sh2} \eta \bar{\rho}_1 \bar{u}_1}{p_{sh1}(1+\eta n_{sh1})} \frac{\partial v_1}{\partial \eta} \right. \\
&\left. + \frac{\rho_{sh1} p_{sh2} \bar{\rho}_1 v_1}{p_{sh1}^2} \frac{\partial v_1}{\partial \eta} \right\} - \frac{2\rho_{sh1} u_{sh1} n_{sh1} \bar{\rho}_1 \bar{u}_1}{p_{sh1}(1+\eta n_{sh1})} \frac{\partial v_2}{\partial \eta} \\
&- \frac{\rho_{sh1} \bar{\rho}_1}{p_{sh1}} \left(v_1 \frac{\partial v_2}{\partial \eta} + v_2 \frac{\partial v_1}{\partial \eta} \right)
\end{aligned} \tag{6}$$

where the terms enclosed by braces are the terms found by Moss,[5,22] Miner and Lewis,[6] and Murray and Lewis,[28] and the remaining terms are due to the second-order expansion of v in Eqs. (4). The resulting second-order terms in the continuity equation along the stagnation streamline ($\xi = 0$) can be combined in the following expression for $v_2(\eta)$:

$$\begin{aligned}
v_2(\eta) = \left(\frac{1}{h_{11}^2 \bar{\rho}} \right) &\left[\bar{\rho}_{1w} v_{2w} - 4\eta u_{sh1} n_{sh2} h_{11} \bar{\rho}_1 \bar{u}_1 \right. \\
&\left. + 2 \frac{n_{sh2}}{n_{sh1}} (h_{11}^2 \bar{\rho}_1 v_1 - \bar{\rho}_{1w} v_{1w}) \right]
\end{aligned} \tag{7}$$

where $v_{1w} = v_{2w} = 0$ for a no-blowing case.

The solution scheme requires that, for each solution iteration along the stagnation streamline, first the $v_{2,\eta}$ distribution is calculated using Eq. (7) and the resulting distribution is numerically differentiated to obtain $v_2(\eta)$ along the stagnation streamline. These v_2 and $v_{2,\eta}$ distributions are then used to obtain the corresponding $\bar{p}_{2,\eta}$ distribution from Eq. (6), which is then numerically integrated from the shock to the body to obtain the required $\bar{p}_2$ distribution along the stagnation streamline. In general, this improved stagnation-point solution is more accurate and results in better behaved distributions of pressure, wall heat transfer, and shock standoff distance in the stagnation region.

Gupta and Simmond[29] have also used a comparable approach to improve the VSL flowfield expansions along the stagnation streamline similar to the earlier approach of Kao.[30] In their approach, the stagnation-point flowfield is expanded in terms of $\sin(s)$, whereas in the present approach, these expansions are directly in terms of the independant variable s [Eqs. (4) and (5)]. Thus, the present approach remains consistent with most of the earlier VSL formulations[5-11,21-26] and provides a means by which they can be extended to higher-order accuracy.

Results and Discussion

In order to evaluate the accuracy of these enhancements in the nonequilibrium VSL scheme, we studied the Mach 20 flow over a sphere-cone configuration under 0- and 20-deg angle-of-attack conditions at an altitude of 175 kft (see Table 1). The sphere-cone configuration considered consists of a 7-deg forecone with a 2-in. nose radius and an overall length of 20 in. (10 nose radii). The wall temperature was assumed to be 2000°R, and the vehicle surface was assumed to be fully catalytic. These test conditions are the same as those used by Buelow et al.[15] and are based on some test cases that we did in an earlier study.[18]

It is important to note that, in our view, the main importance and usefulness of the VSL scheme is in generating the starting solutions for more accurate and robust afterbody solution schemes (such the PNS schemes). Although the VSL solution scheme is indeed quite applicable in the afterbody region, there are some important issues that also need to be properly addressed in order to maintain solution accuracy under high-altitude (low Reynolds number) conditions. For example, under such conditions, if the input shock shape was generated using an inviscid approach (which is usually the case), it needs to be improved by performing the necessary global iterations. Needless to say, these global iterations may not be easy to do (as it turned out to be the case for the present test cases). In this study, no VSL global iterations were done, and the afterbody VSL solutions were only done in order to provide an additional set of predictions to be compared with the corresponding afterbody PNS predictions.

The results of these test cases are discussed in the following sections. Where possible, these nonequilibrium VSL predictions are checked for accuracy by comparing with the corresponding predictions of the nonequilibrium Navier-Stokes solution scheme of Molvik and Merkle,[2] our three-dimensional nonequilibrium PNS scheme,[18] and the upwind PNS scheme of Buelow et al.[15]

Zero Angle-of-Attack Test Case (Case 1)

For clarity, the results of this zero angle-of-attack test case are separated into the blunt-body region and the afterbody region.

Blunt-Body Flowfield Region

The main focus of the present study is the importance of accurately satisfying the conservation of element mass in the nonequilibrium VSL scheme. It is important to note that in the VSL solution scheme the global conservation of mass is dictated by the continuity equation and enforced in part by updating the shock standoff distance based on an integrated form of the continuity equation (the shock slope remains unchanged during this process). As long as the input shock shape and the continuity equation are not changed, the global conservation of mass cannot be affected. However, in the nonequilibrium case, the final error in the global conservation of mass is an algebraic sum of individual errors in the conservation of element mass. These nonconservative errors can be

Table 1 Freestream conditions

Quantity	
Mach number	20.000
Reynolds number	1.34E + 4
Pressure, lb/ft^2	1.102
Density, slug/ft^3	1.32E − 6
Temperature, °R	485.151
Velocity, ft/s	2.16E + 4
Angle of attack, deg	
Case 1	0.000
Case 2	20.000
Wall temperature, °R	2000.00
Nose radius, in.	2.00

of different signs and, thus, can be numerically much larger than the final error in the global conservation of mass.

For example, for these case 1 calculations, the error in the global conservation of mass at $s/Rn = 1.6$ was approximately +6% of the freestream mass flux. Without enforcing the element conservation equations, at the same location the error in the global conservation of N atoms was + 11% and that of O atoms was − 5% (+11% − 5% = 6%). However, when the conservation equations of N and O atoms were also enforced, at the same location the error in the global conservation of N atoms was approximately + 3.5% and that of O atoms was approximately +2.5% (+3.5% + 2.5% = 6%). As can be seen, with the present approach of enforcing the element conservation, although the overall global conservation of mass error does not change (because the shock shape and the continuity equation do not change), the individual errors in the conservation of element mass did improve. Figure 2 shows the mass fraction of O atoms at this location with and without forcing the conservation of element mass. With the present approach, the mass fraction of O is almost constant at 0.23456 across the entire shock layer, whereas the previous VSL predictions were significantly lower in the peak temperature region.

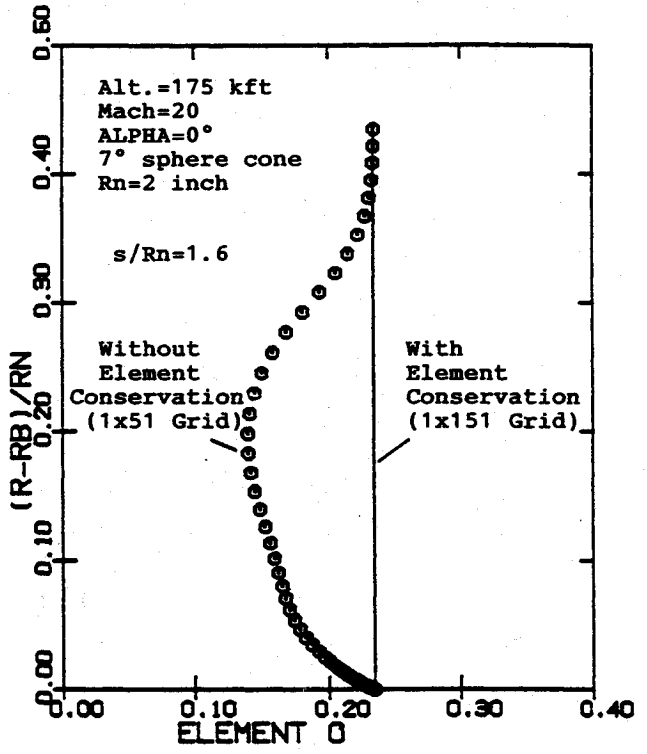

Fig. 2 Effects of imposing the element conservation equations on the mass fraction of oxygen atoms for case 1.

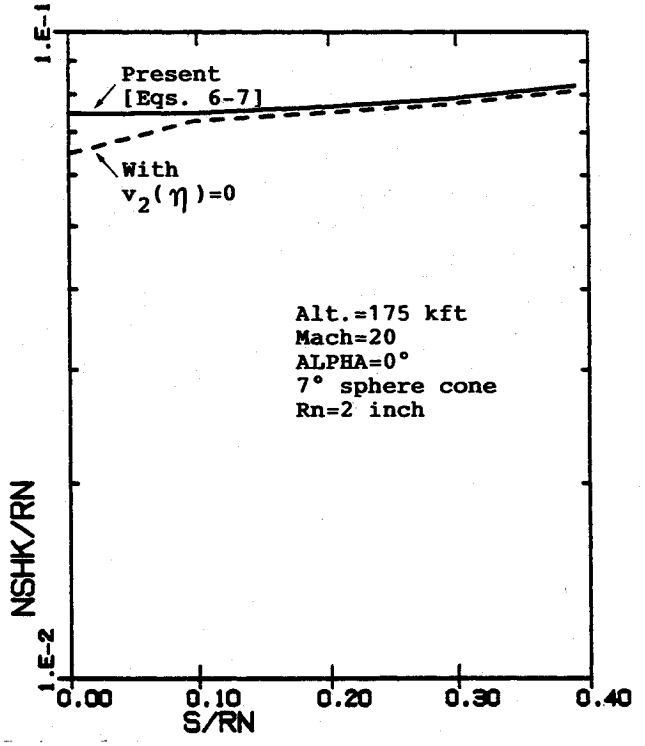

Fig. 3 Effects of second-order $v(\eta)$ expansion on the predicted shock standoff distance in the stagnation region for case 1.

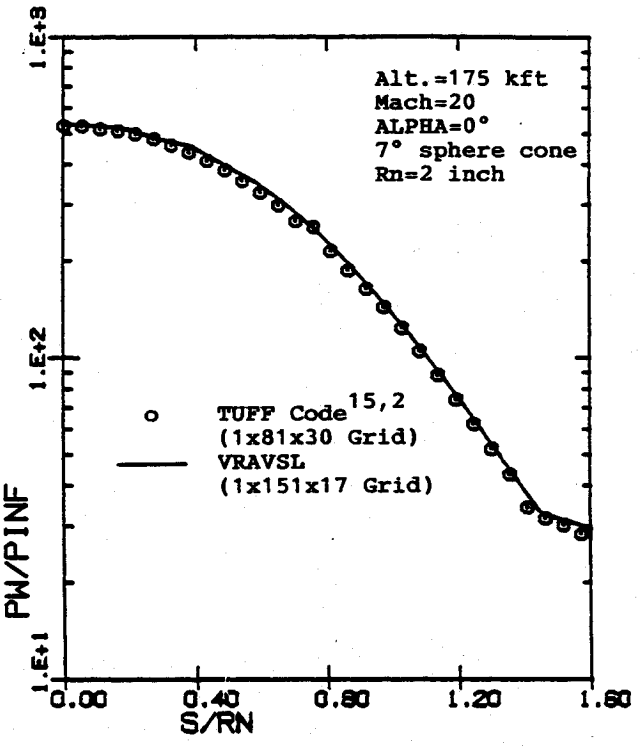

Fig. 4 Comparison of surface pressure in the blunt-body region for case 1.

The effects of the improved $v(\eta)$ expansion [Eqs. (4)] on the flowfield in the stagnation region are shown in Fig. 3. Without the second-order modifications, the shock standoff distance (n_{shk}) at the stagnation point is significantly underpredicted and its distribution in the vicinity of the stagnation point is not smooth and well behaved (Fig. 3). With the proposed second-order extensions [Eqs. (4–7)], this nonphysical behavior is eliminated, resulting in smoother flowfield and (n_{shk}) variations in the stagnation region (Fig. 3).

The VSL predictions of the flowfield and chemistry in the blunt-body region are compared in Figs. 4–7 with the corresponding predictions of the TUFF (Navier-Stokes) code of Molvik and Merkle.[2] These TUFF calculations were done by Buelow et al.[15] and provided to us. These case 1 VSL calculations were done using 151 grid points between the body and the shock, whereas the TUFF calculations were done using 81 points between the body and the outer freestream boundary. The VSL prediction of the surface pressure in the blunt-body region is compared with the TUFF prediction in Fig. 4 and shows excellent agreement. The corresponding heat transfer and skin-friction predictions from the TUFF code were not available and, thus, could not be compared.

The temperature profiles along the stagnation streamline are compared in Fig. 5 and show excellent agreement between the VSL and TUFF predictions. These figures also show that the predicted VSL shock standoff distance is in good agree-

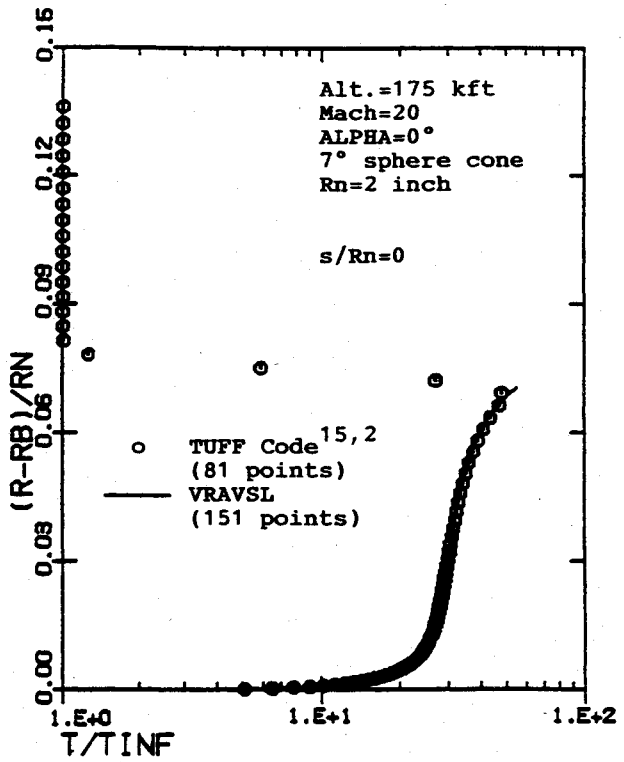

Fig. 5 Comparison of temperature profiles at $s/Rn = 0$ for case 1.

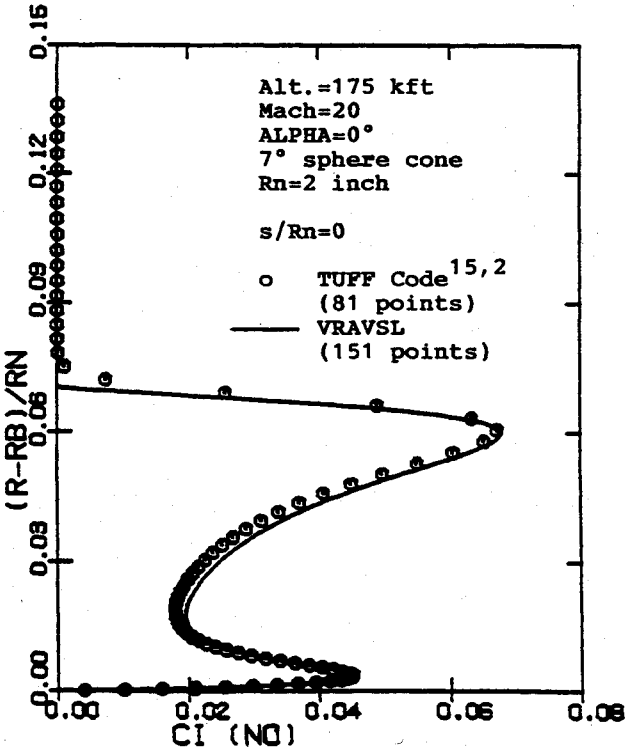

Fig. 6 Comparison of NO concentration profiles at $s/Rn = 0$ for case 1.

ment with the bow shock captured by the TUFF code. The corresponding NO and NO^+ concentration profiles are generally in very good agreement (Figs. 6 and 7), except for the peak concentration region where the TUFF predictions are 20–25% higher.

The flowfield and species profiles from the VSL and TUFF calculations at $s/Rn = 1.5708$ ($x/Rn = 1.0$) are compared in Figs. 8–11. The pressure and temperature profiles (Figs. 8 and 9) show that, in general, the agreement in the near-wall as well as the outer flow region is very good. There are, however, some small differences in the location of the bow shock and, thus, the conditions immediately behind the bow shock. It is fair to say that at this location, due to the tangent-point discontinuity, the VSL shock standoff predictions may not be very accurate, but at the same time, the TUFF results show the predicted bow shock to be slightly smeared. In any case, these differences are still small in magnitude and effect.

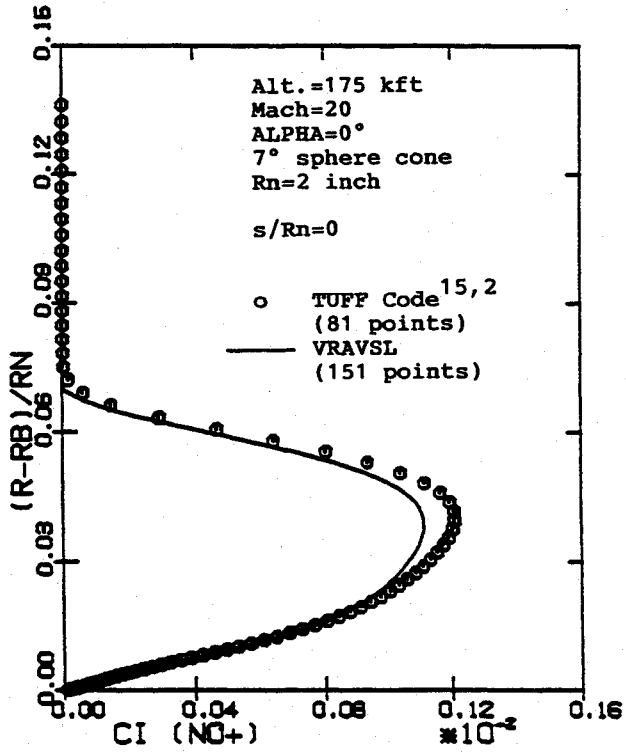

Fig. 7 Comparison of NO^+ concentration profiles at $s/Rn = 0$ for case 1.

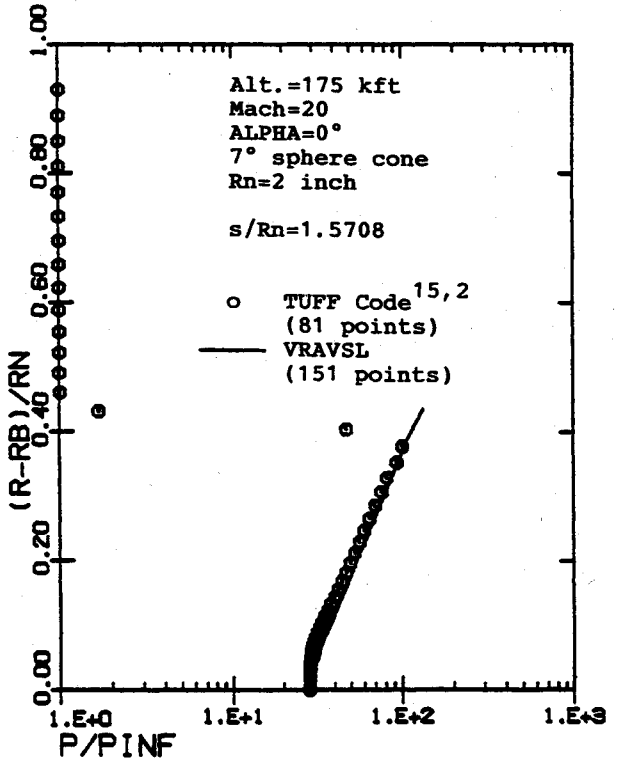

Fig. 8 Comparison of pressure profiles at $s/Rn = 1.5708$ for case 1.

The NO and NO^+ species profiles at this location are compared in Figs. 10 and 11 and show that the agreement between the VSL and TUFF predictions is generally very good. There are some small differences (approximately 20%) in the predicted peak concentration levels. Furthermore, compared to the VSL predictions, the TUFF results show a slightly thinner layer of dissociated and ionized air, but this could also simply

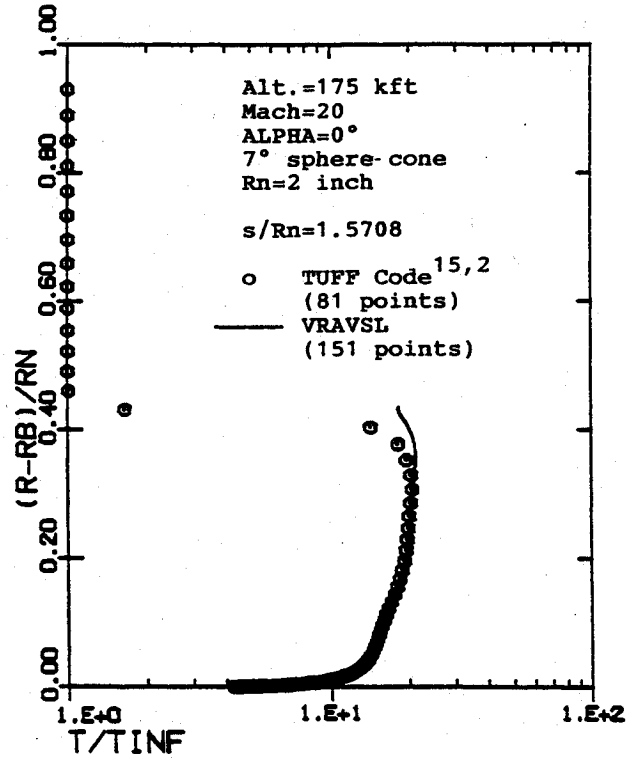

Fig. 9 Comparison of temperature profiles at $s/Rn = 1.5708$ for case 1.

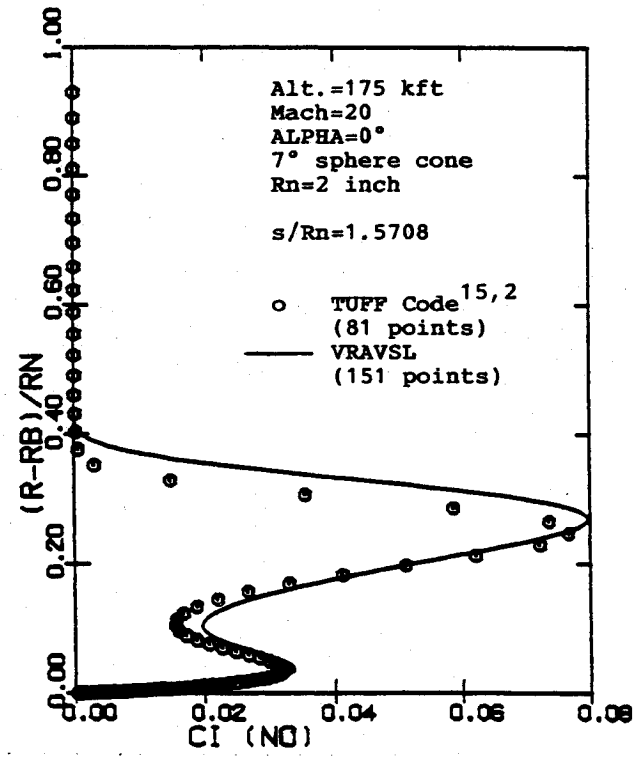

Fig. 10 Comparison of NO concentration profiles at $s/Rn = 1.5708$ for case 1.

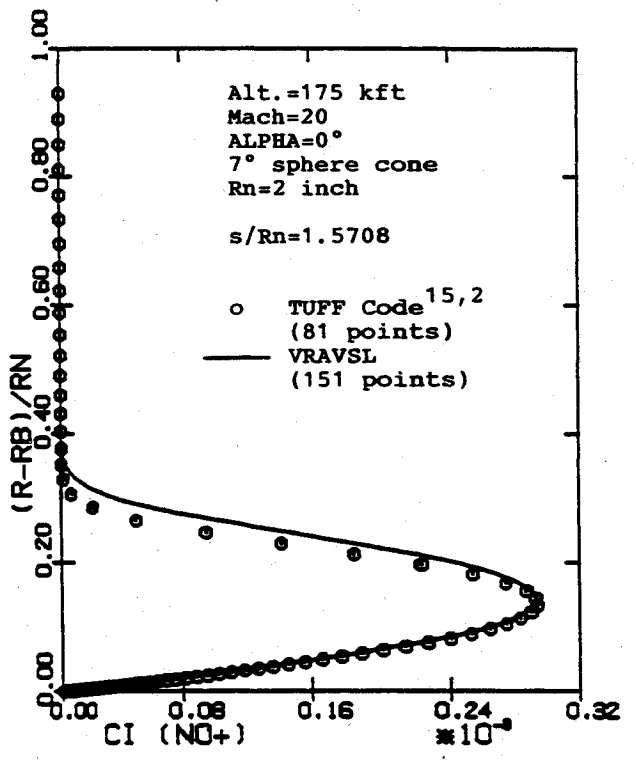

Fig. 11 Comparison of NO^+ concentration profiles at $s/Rn = 1.5708$ for case 1.

Table 2 Computing times

Case	Numerical scheme	x/Rn, From-to	Grid,[c] $N1 \times N2 \times N3$	CPU time,[d] m:s
1	VRAVSL[a]	0.0 – 1.00	17 × 151 × 1	0:10
	VRAVSL	0.0 – 10.0	50 × 151 × 1	0:30
	VRAPNS[b]	1.1 – 10.0	25 × 151 × 1	0:20
2	VRAVSL	0.0 – 2.50	20 × 50 × 9	0:30
	VRAVSL	0.0 – 10.0	35 × 50 × 9	1:00
	VRAPNS	1.2 – 10.0	22 × 50 × 31	3:00

[a]VRAVSL = three-dimensional viscous shock-layer solution.
[b]VRAPNS = three-dimensional parabolized Navier-Stokes solution.
[c]$N1$ = number of streamwise marching steps; $N2$ = number of points between body and shock; $N3$ = number of equally spaced crossflow planes.
[d]Equivalent computing time on Cray Y/MP with CFT77 compiler and auto vectorization.

be a reflection of the differences in the predicted shock standoff distance.

The computing times and grid used for this VSL blunt-body solution are shown in Table 2, which shows that this VSL blunt-body calculation took only 11 s on Cray Y/MP. On the other hand, although the computing time required by the TUFF calculations is not available, Buelow et al.[15] have reported that these TUFF calculations took 1500 iterations to converge. It is clear that, for spherical nose tips, the present nonequilibrium VSL scheme is an accurate and efficient approach for generating the blunt-body flowfield.

Afterbody Flowfield Region

The VSL solution for case 1 conditions was also done over the entire blunt-body and afterbody region. These VSL predictions of the wall heat transfer rate are compared in Fig. 12 with the corresponding predictions of our nonequilibrium VRAPNS (VRA, Inc., PNS) code[18] using 150 points between the body and the shock. The starting solution for this VRAPNS calculation was located at $x = 1Rn$, and was generated using the present nonequilibrium VSL blunt-body solution. These results show excellent agreement between the VSL and VRAPNS predictions over the entire body length.

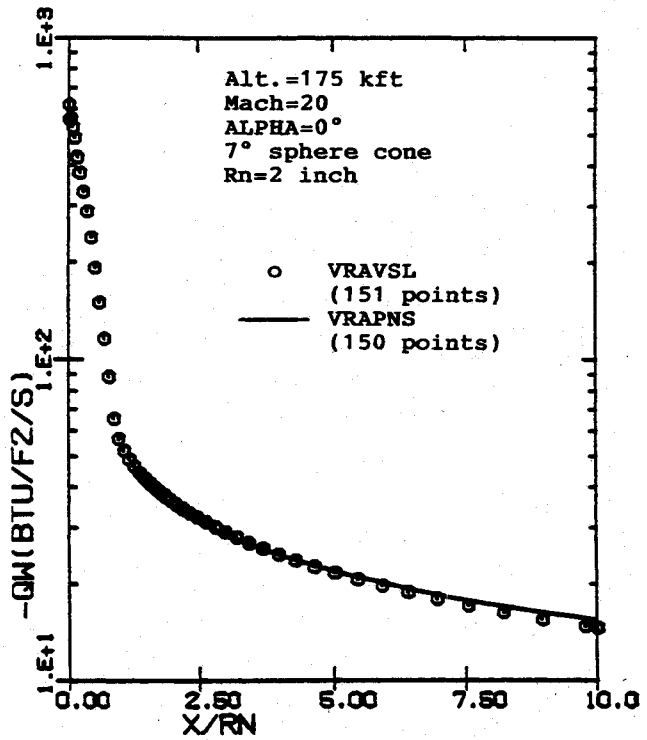

Fig. 12 Comparison of wall heat transfer rate in the afterbody region for case 1.

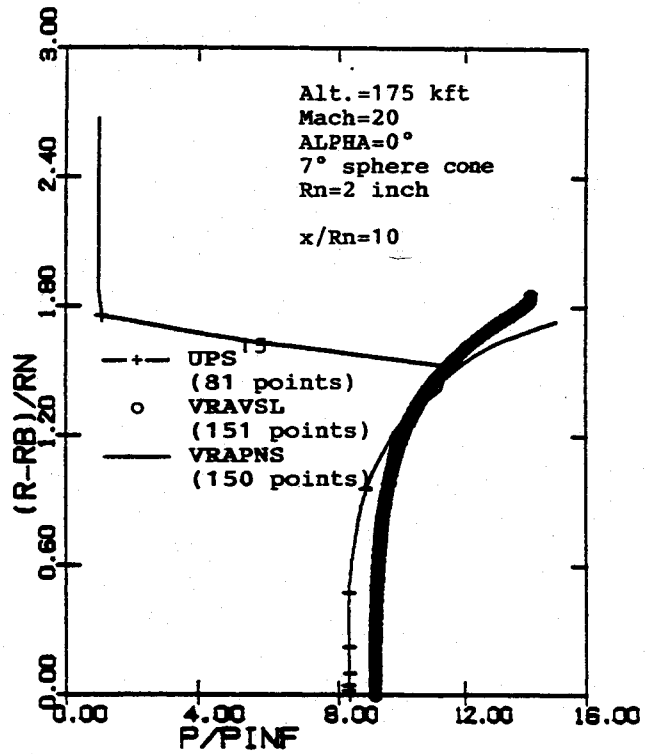

Fig. 13 Comparison of pressure profiles at $x/Rn = 10$ for case 1.

Buelow et al.[15] have also done upwind parabolized Navier-Stokes (UPS) calculations for this case using the TUFF solution to start their afterbody UPS code. The pressure profiles at the body end ($x = 10Rn$) are compared in Fig. 13 and show that the VSL and VRAPNS predictions are in excellent agreement with each other. There are some differences immediately behind the bow shock due to the larger shock standoff distance predicted by the VSL; however, these differences vanish very quickly. It should be pointed out that the VRAPNS scheme involves an implicit shock-fitting approach in which the shock shape is predicted as part of the marching solution. It is interesting to note that the UPS predictions of the start of the captured bow shock wave are in excellent agreement with the VRAPNS predictions. However, the UPS prediction of the wall pressure is approximately 10% lower than the corresponding VRAPNS and VSL predictions. It should also be noted that Fig. 4 shows that the wall-pressure prediction of the TUFF code (used to start the UPS code) is in excellent agreement with the blunt-body VSL prediction (used to start the VRAPNS code). Thus, it is our view that these differences in the afterbody region are caused by the UPS predictions.

The temperature profiles shown in Fig. 14 show that the VRAPNS and VSL predictions are almost identical over most of the shock layer, with some differences in the outer region that are again due to the difference in the predicted shock standoff distance and shock slope. The UPS predictions are in agreement with the VSL and VRAPNS predictions in the near-wall region; however, UPS predicts about a 15% higher peak temperature and a much thinner high-temperature layer. It is interesting to note that the UPS predictions of the bow shock are smeared over approximately 20% of the shock-layer thickness, and this may be a major reason for these differences.

The NO and NO^+ species profiles at the body end ($x = 10$ Rn) are compared in Figs. 15 and 16. In general, the VSL and VRAPNS predictions are in very good agreement with each other, except for some small (about 20%) differences in the predicted peak concentration levels. The UPS predictions are in close agreement with these VSL and VRAPNS predictions in the near-wall region. In the outer shock-layer region, the UPS predictions differ somewhat from these VSL and VRAPNS predictions, but these differences are primarily due to the thinner shock layer predicted by the UPS scheme.

It should be noted that the only differences in the nonequilibrium VRAPNS results of Ref. 18 and the present VRAPNS predictions are caused by the differences in the starting VSL blunt-body solution. Since the body length is quite short (in terms of nose radii), the starting solution does have a significant effect on the flowfield at the body end. The computing times for these VSL and VRAPNS calculations are shown in Table 2.

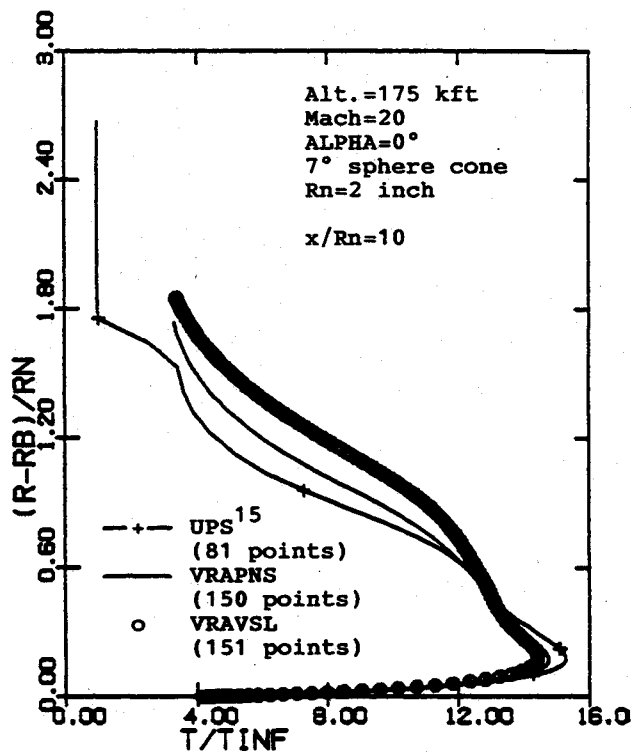

Fig. 14 Comparison of temperature profiles at $x/Rn = 10$ for case 1.

20-Degree Angle-of-Attack Test Case (Case 2)

The 20-deg angle-of-attack (case 2) calculations were done using VSL and VRAPNS solution schemes. Briefly speaking, the VSL calculations were done using nine crossflow planes and 51 points between the body and the shock. The corresponding VRAPNS calculations were done using 31 crossflow planes and 50 points between the body and the shock. The grids used and the corresponding computing times for these case 2 calculations are shown in Table 2.

In evaluating these VSL results, it should be noted that, when crossflow separation begins on the leeside at large angles of attack, the VSL solution scheme (due to its parabolic crossflow nature) cannot march through this crossflow separated region and, thus, drops these leeside solution planes. Actually, this leeside VSL solution remains attached for some short

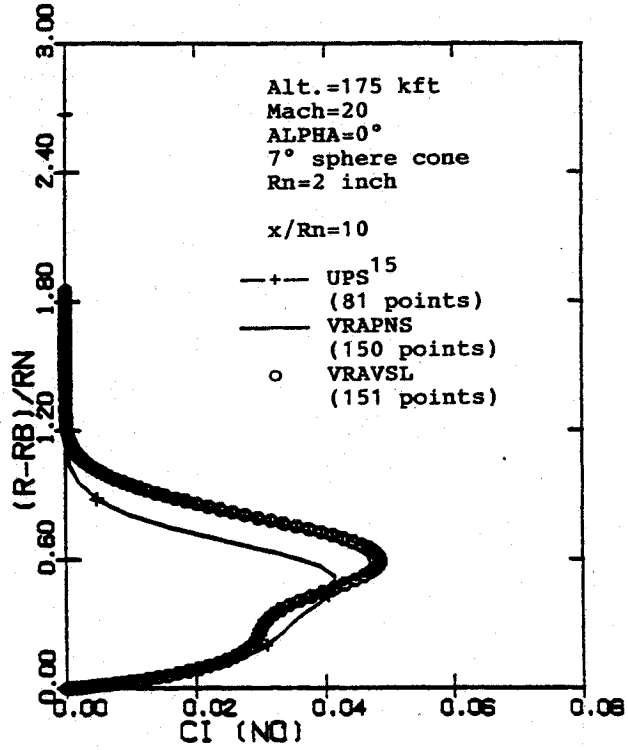

Fig. 15 Comparison of NO concentration profiles at $x/Rn = 10$ for case 1.

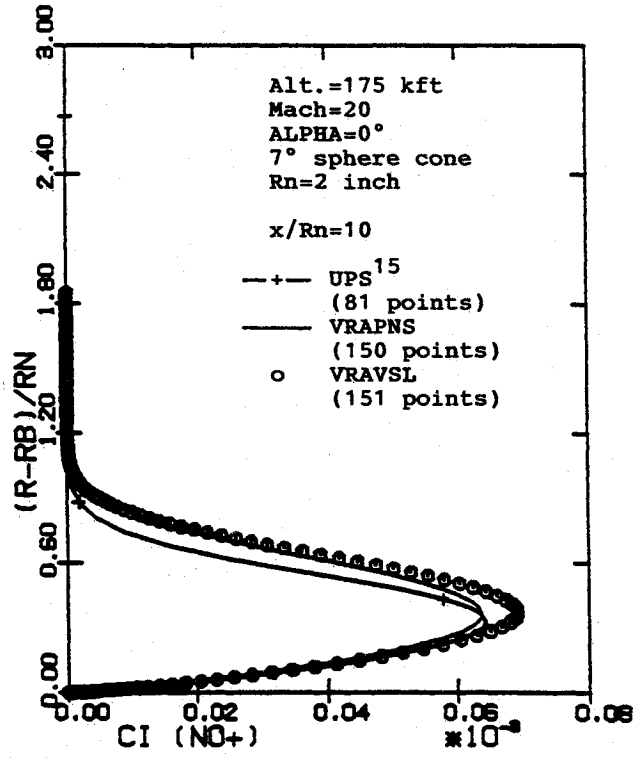

Fig. 16 Comparison of NO^+ concentration profiles at $x/Rn = 10$ for case 1.

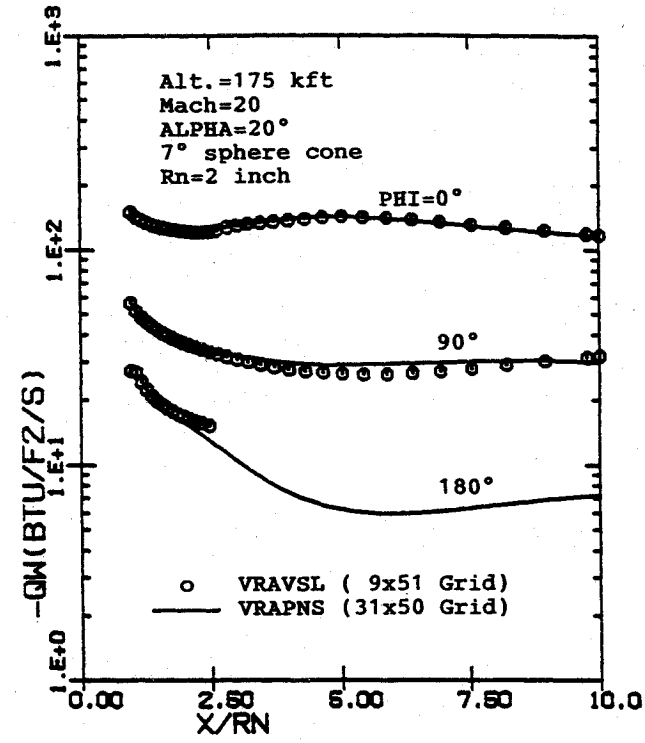

Fig. 17 Comparison of the axial distribution of wall heat transfer rate for case 2.

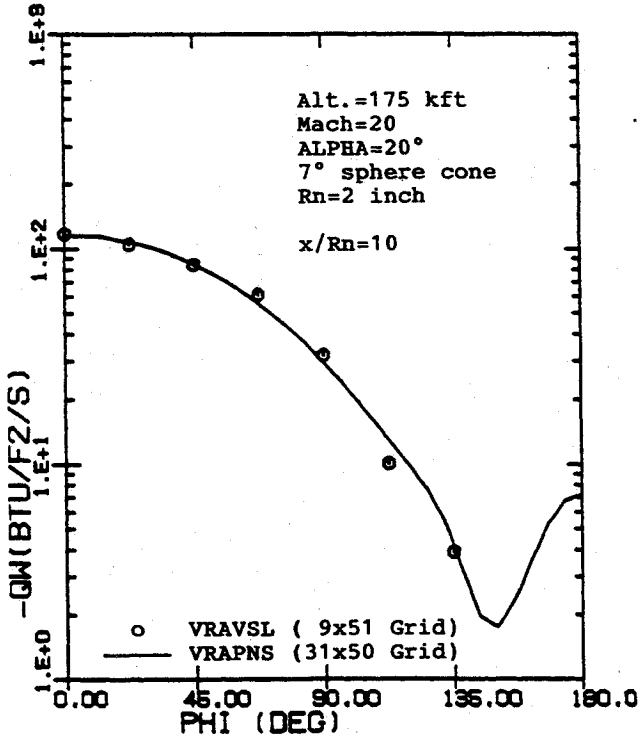

Fig. 18 Comparison of the crossflow distribution of wall heat transfer rate at $x/Rn = 10$ for case 2.

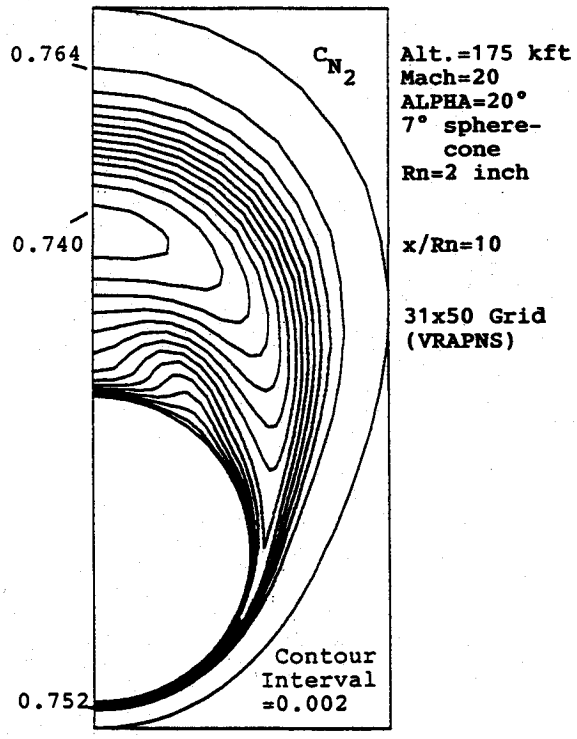

Fig. 19 N_2 concentration contours at $x/Rn = 10$ for case 2.

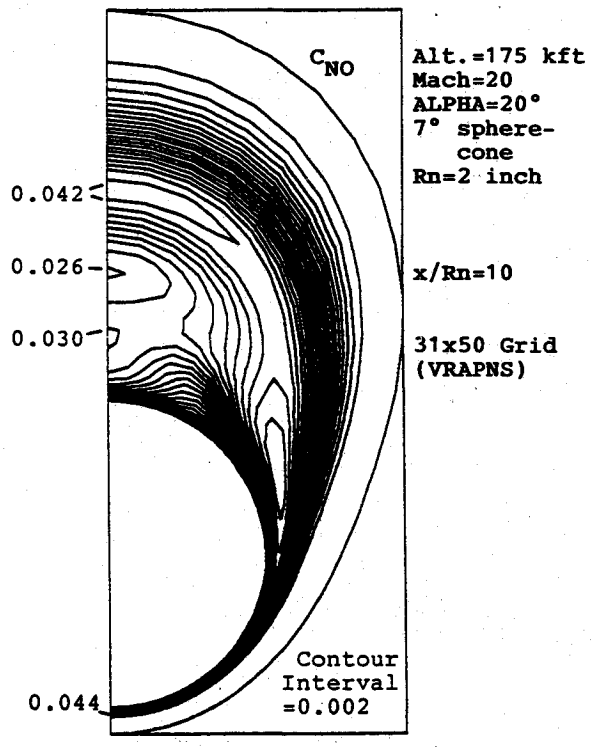

Fig. 20 NO concentration contours at $x/Rn = 10$ for case 2.

distance before it encounters numerical difficulties and drops these troublesome leeside solution planes. For example, for these case 2 calculations, the VRAPNS calculations show that crossflow separation on the leeside starts somewhere between $x = 2Rn$ and $2.5Rn$. Although in this region the present VSL solution remains attached (maybe due to the coarse nine-plane grid), it is not expected to be very accurate. It should be mentioned that the initial data plane (IDP) for these VRAPNS calculations was generated at $x = 1.1Rn$ using the corresponding VSL blunt-body solution.

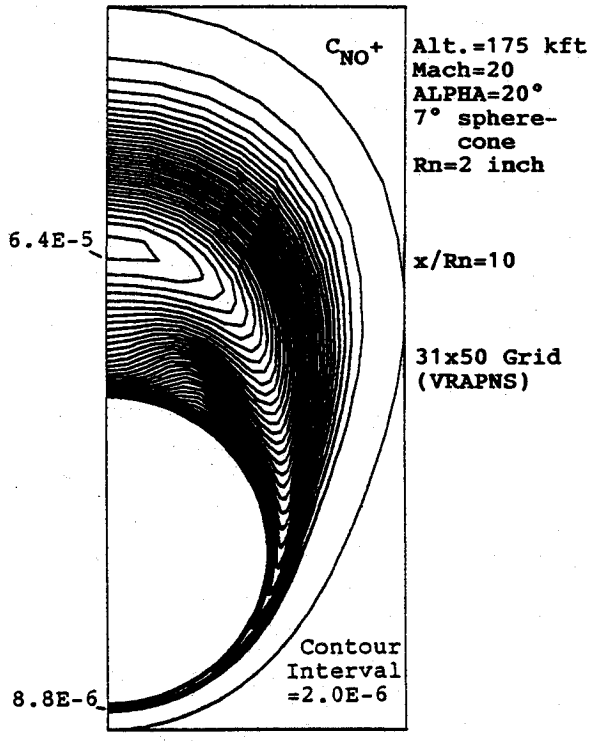

Fig. 21 NO^+ concentration contours at $x/Rn = 10$ for case 2.

The axial distributions of the wall heat transfer rate along the windward ($\phi = 0$ deg), side ($\phi = 90$ deg), and leeward ($\phi = 180$ deg) planes are shown in Fig. 17, and the corresponding crossflow distributions at the body end are shown in Fig. 18. There is excellent agreement along the windward streamline, and the predicted surface heating along the side ($\phi = 90$ deg) is within 10% of each other. As mentioned before, this three-dimensional VSL solution was not globally iterated and, thus, the predicted shock-layer thickness is slightly thicker than the corresponding VRAPNS predictions. These observed differences in the surface heating, although small, are primarily due to this difference in the shock-layer thickness. In general, until the start of the crossflow separated region, the VSL and VRAPNS predictions are in excellent agreement with each other. It is indeed refreshing to note this close agreement in these predictions, especially in view of the coarse VSL grid in the crossflow direction. Sample contours of the N_2, NO, and NO^+ species mass fractions at the body end obtained using the VRAPNS predictions are shown in Figs. 19–21. These figures show that the predicted species concentrations are quite well behaved and smooth.

Conclusions

In this study, we have enhanced the existing nonequilibrium VSL solution scheme to improve its solution accuracy in the stagnation region and also minimize and control errors in the conservation of elemental mass. The stagnation-point solution is improved by using a second-order expansion for the normal velocity, and the elemental mass conservation is improved by directly imposing the element conservation equations. The modifications are such that the general structure and computational efficiency of the nonequilibrium VSL scheme are not affected. The Mach 20 flow over a 7-deg sphere-cone vehicle is studied at 0- and 20-deg angles of attack. Comparisons are made with the available predictions from Navier-Stokes and parabolized Navier-Stokes solution schemes. The results of this study substantiate the following comments:

1) The solution accuracy of the nonequilibrium VSL scheme is significantly enhanced by imposing the element conservation equations instead of some of the species conservation equations.

2) The flowfield and chemistry predictions of the improved nonequilibrium blunt-body VSL scheme are in excellent agreement with corresponding predictions of the nonequilibrium Navier-Stokes (TUFF) code of Molvik and Merkle.[2]

3) In the afterbody region, the flowfield and chemistry predictions of this improved nonequilibrium VSL scheme are in good-to-excellent agreement with corresponding predictions of the nonequilibrium parabolized Navier-Stokes schemes of Bhutta and Lewis[18] and Buelow et al.[15] In general, the agreement is better with the VRAPNS scheme of Bhutta and Lewis,[18] whereas the UPS scheme of Buelow et al.[15] tends to predict a more diffused bow shock and, consequently, a thinner shock layer.

4) For short bodies (in terms of nose radii), the effects of the starting solution on the PNS afterbody solution schemes are significant, and the accuracy of the blunt-body solution scheme used to generate this starting solution cannot be ignored.

5) With solution enhancements, the nonequilibrium blunt-body VSL scheme remains an accurate, fast, and extremely efficient means for generating the blunt-body flowfield over spherical nose tips at zero-to-large angles of attack. These VSL blunt-body solutions can then be reliably used to start a more accurate afterbody PNS scheme.

Acknowledgments

The work reported in this paper was supported in part by NASA Lewis Research Center under Contract NAS3-25450. The encouragement and cooperation provided by Louis Povinelli, Dan Whipple, and the contract monitor Tom Benson during the course of this effort are gratefully acknowledged. The authors would also like to thank J. Tannehill and his colleagues at Engineering Analysis, Inc., Ames, Iowa, and Iowa State University, Ames, Iowa, for their help in obtaining the detailed TUFF and UPS results used in this study for comparison purposes.

References

[1]Blottner, F. G., Johnson, M., and Ellis, M., "Chemically Reacting Viscous Flow Program for Multi-Component Gas Mixtures," Sandia National Laboratories, Rept. SC-RR-70-754, Albuquerque, NM, Dec. 1971.

[2]Molvik, G. A., and Merkle, C. L., "A Set of Strongly-Coupled Upwind Algorithms for Computing Flows in Chemical Nonequilibrium," AIAA Paper 89-0199, Jan. 1989.

[3]Candler, G., "On the Computation of Shock Shapes in Nonequilibrium Hypersonic Flows," AIAA Paper 89-0312, Jan. 1989.

[4]Gnoffo, P. A., "Code Calibration in Support of the Aeroassist Flight Experiment," *Journal of Spacecraft and Rockets,* Vol. 27, No. 2, 1990, pp. 131–142.

[5]Moss, J. N., "Reacting Viscous Shock-Layer Solutions with Multicomponent Diffusion and Mass Injection," NASA TR-R-411, June 1974.

[6]Miner, E. W., and Lewis, C. H., "Hypersonic Ionizing Air Viscous Shock-Layer Flows over Nonanalytic Blunt Bodies," NASA CR-2550, May 1975.

[7]Swaminathan, S., Kim, M. D., and Lewis, C. H., "Nonequilibrium Viscous Shock-Layer Flows over Blunt Sphere-Cones at Angles of Attack," AIAA Paper 82-0825, June 1982.

[8]Shinn, J. L., Moss, J. N., and Simmonds, A. L., "Viscous Shock-Layer Heating Analysis for the Shuttle Windward Plane with Surface Finite Catalytic Recombination Rates," AIAA Paper 82-0842, June 1982; also, *Entry Vehicle Heating and Thermal Protection Systems, Space Shuttle, Solar Starprobe, Jupiter, Galileo Probe,* edited by P. E. Bauer and H. E. Collicott, Vol. 85, Progress in Astronautics and Aeronautics, AIAA, New York, 1985, pp. 149–180.

[9]Kim, M. D., Swaminathan, S., and Lewis, C. H., "Three-Dimensional Nonequilibrium Viscous Flow Computations past the Space Shuttle," AIAA Paper 83-0487, Jan. 1983.

[10]Song, D. J., and Lewis, C. H., "Hypersonic Finite-Rate Chemically Reacting Viscous Flows over an Ablating Carbon Surface," *Journal of Spacecraft and Rockets,* Vol. 23, No. 1, 1986, pp. 47–54.

[11]Thompson, R. A., "Comparisons of Nonequilibrium Viscous Shock-Layer Solutions with Windward Surface Shuttle Heating Data," AIAA Paper 87-1473, June 1987.

[12]Gupta, R. N., "Stagnation Flowfield Analysis for an Aeroassist Flight Experiment Vehicle," AIAA Paper 88-2613, June 1988.

[13]Zoby, E. V., Lee, K. P., Gupta, R. N., Thompson, R. A., and Simmonds, A. L., "Viscous Shock-Layer Solutions with Nonequilibrium Chemistry for Hypersonic Flows past Slender Bodies," *Journal of Spacecraft and Rockets,* Vol. 26, No. 4, 1989, pp. 221–228.

[14]Bhutta, B. A., Song, D. J., and Lewis, C. H., "Nonequilibrium Viscous Hypersonic Flows over Ablating Teflon Surfaces," *Journal of Spacecraft and Rockets,* Vol. 27, No. 2, 1990, pp. 205–215; also, AIAA Paper 89-0314, April 1989.

[15]Buelow, P., Ievalts, J., and Tannehill, J., "Comparison of Three-Dimensional PNS Codes," AIAA Paper 90-1572, June 1990.

[16]Edwards, T. A., and Flores, J., "Computational Fluid Dynamics Nose-to-Tail Capability: Hypersonic Unsteady Navier-Stokes Code Validation," *Journal of Spacecraft and Rockets,* Vol. 27, No. 2, 1990, pp. 123–130.

[17]Ryan, J. S., Flores, J., and Chow, C.-Y., "Development and Validation of a Navier-Stokes Code for Hypersonic External Flows," *Journal of Spacecraft and Rockets,* Vol. 27, No. 2, 1990, pp. 160–166.

[18]Bhutta, B. A., and Lewis, C. H., "Three-Dimensional Hypersonic Nonequilibrium Flows at Large Angles of Attack," *Journal of Spacecraft and Rockets,* Vol. 26, No. 3, 1989, pp. 158–166; also, AIAA Paper 88-2568, June 1988.

[19]Bhutta, B. A., and Lewis, C. H., "Low Reynolds Number Flows past Complex Multiconic Geometries," AIAA Paper 85-0362, Jan. 1985.

[20]Bhutta, B. A., Lewis, C. H., and Kautz, F. A., II, "A Fast Fully-Iterative Parabolized Navier-Stokes Scheme for Chemically-Reacting Reentry Flows," AIAA Paper 85-0926, June 1985.

[21]Davis, R. T., "Hypersonic Flow of a Chemically Reacting Binary Mixture past a Blunt Body," AIAA Paper 70-805, July 1970.

[22]Moss, J. N., "Solutions for Reacting and Nonreacting Viscous Shock Layers with Multicomponent Diffusion and Mass Injection," Ph.D. Dissertation, Virginia Polytechnic Inst. and State Univ., Blacksburg, VA, Oct. 1971.

[23]Swaminathan, S., Kim, M. D., and Lewis, C. H., "Real Gas Flows over Complex Geometries at Moderate Angles of Attack," *Journal of Spacecraft and Rockets,* Vol. 20, No. 4, 1983, pp. 321–322; also, AIAA Paper 82-0392, Jan. 1982.

[24]Swaminathan, S., Kim, M. D., and Lewis, C. H., "Three-Dimensional Nonequilibrium Viscous Shock-Layer Flows over Complex Geometries," *AIAA Journal,* Vol. 22, No. 6, 1984, pp. 754–755; also, AIAA Paper 83-0212, Jan. 1983.

[25]Waskiewicz, J. D., and Lewis, C. H., "Recent Developments in Viscous Shock-Layer Theory," Virginia Polytechnic Inst. and State Univ., VPI&SU AERO-079, Blacksburg, VA, March 1978.

[26]Kim, M. D., Bhutta, B. A., and Lewis, C. H., "Three-Dimensional Effects upon Real Gas Flows past the Space Shuttle," AIAA Paper 84-0225, Jan. 1984.

[27]Bird, R. B., Stewart, W. E., and Lightfoot, E. N., *Transport Phenomena,* Wiley, New York, 1960.

[28]Murray, A. L., and Lewis, C. H., "Hypersonic Three-Dimensional Viscous Shock-Layer Flows over Blunt Bodies," *AIAA Journal,* Vol. 16, No. 12, 1978, pp. 1279–1286.

[29]Gupta, R. N., and Simmond, A. L., "Hypersonic Low-Density Solutions of the Navier-Stokes Equations with Chemical Nonequilibrium and Multicomponent Surface Slip," AIAA Paper 86-1349, June 1986.

[30]Kao, H. C., "Hypersonic Viscous Flow near the Stagnation Streamline of a Blunt-Body: I.—A Test of Local Similarity," *AIAA Journal,* Vol. 2, No. 11, 1964, pp. 1892–1897.

Ernest V. Zoby
Associate Editor